UNIVERSITY OF LEEDS

White Rose
university consortium
Universities of Leeds, Sheffield & York

eprints@whiterose.ac.uk
https://eprints.whiterose.ac.uk/

Revealing the temperature effects on the corrosion behaviour of 2205 duplex stainless steel from passivation to activation in a CO_2-containing geothermal environment

Huifeng Liu[a,c], Jianbo Sun[a*], Jiong Qian[b], Baoshun Wang[b], Shengkai Shi[a], Yu Zhu[a], Yong Wang[a], Anne Neville[c] and Yong Hua[c*]

[a]: School of Materials Science and Engineering, China University of Petroleum (East China), Qingdao, China

[b]: Corrosion and Integrity Centre, Zhejiang JIULI Hi-Tech Metals Co. Ltd, Hang Zhou, China.

[c]: Institute of Functional Surfaces, School of Mechanical Engineering, University of Leeds, LS2 9JT, United Kingdom

*Corresponding author: Yong Hua, E-mail address: Y.Hua@leeds.ac.uk.

Jianbo Sun, E-mail address: sunjianbo@upc.edu.cn.

Abstract

The temperatures and pressures influencing the formation mechanism of the passive film and corrosion products, as well as passivation performance of 2205 duplex stainless steel (DSS), were systematically studied via immersion tests, electrochemical measurements, and various advanced surface techniques. The results indicate that the passive film at 150°C was an amorphous structure, while the corrosion products were comprised of nano-polycrystalline $FeCr_2O_4$, $CrOOH$, and $NiFe_2O_4$ at 300°C. A Ni-rich layer was observed at the inner interface in both temperatures. A thermodynamic assessment was to validate the experimental results and reveal fundamental corrosion mechanisms of 2205 DSS exposed to the geothermal environments.

Keywords: 2205 duplex stainless steel, passive film, geothermal, thermodynamic

1.Introduction

The global energy situation and environmental issues caused by the use of fossil energy have encouraged the world to find new alternative energy sources to establish a diversified energy

28   structure. To achieve "net-zero" carbon emissions which have become the goal of most developed

29   nations in a time frame from 2035 to 2050. With abundant reserves and low carbon emissions,

30   geothermal energy is attracting more attention [1]. It is estimated that the geothermal energy stored

31   on the earth is about 14.5×10^{25} J, which is equivalent to 4948 trillion tons of coal compared to the

32   global coal burial of 1 trillion tons [2]. The use of geothermal energy reduces the annual carbon

33   dioxide by 80 Mt [3], which greatly decreases the greenhouse gas effect. The harsh environmental

34   conditions of geothermal exploitation have exposed large restrictions to the application of the

35   materials in the past decades [4]. Because of the focus on the long-term service life under harsh high-

36   temperature and high-pressure environments, deterioration of materials such as corrosion or

37   material degradation becomes a key issue affecting the safe application of geothermal production

38   and greatly increases the maintenance costs.

39   Numerous corrosion-resistance alloys (CRAs) such as martensitic, austenitic, and duplex stainless

40   steel (DSS) and Nickel-based [5-16] have been tested in both laboratories and field environments.

41   Among them, 2205 DSS provides good corrosion resistance and relatively low cost, which has

42   become the alternative option for the geothermal environments containing concentrated Cl^- and

43   high levels of CO_2 [5]. The microstructure of 2205 DSS has around 50% ferrite and 50% austenite

44   phases. To achieve 50% austenite requires high chromium content and low nickel content, the

45   presence of 3 wt.% molybdenum can reduce the susceptibility of pitting or stress corrosion cracking

46   [6, 7].

47   For a geothermal environment, one of the main considerations influencing the protection

48   performance of the passive film or accelerating the formation of the corrosion product is

49   temperature. Many researchers have reported that the increase of temperature results in the failure

50   of the passive film and the development of localized corrosion is caused by the accumulation and

51   adsorption of chloride ions (Cl^-) at the metal surface [9-13]. Increasing temperature accelerates the

52   rate of electrochemical reactions as well as metal ion diffusion within the system [5]. The study by

53   Okoro et al. [8] showed that the corrosion rate of CO_2-containing pipelines increased with

54   temperatures, and the corrosion rates almost double for every 6°C increase in temperature. Zhao et

55   al. [14] simulated a CO_2 corrosion environment in oil and gas wells and found that the passive film on

56   the surface of HP-13Cr stainless steel transformed into complex corrosion product layers as the

57   temperature increased from 95 °C to 180 °C. Yue et al. [16] reported that an amorphous passive film

58   mainly containing $Cr(OH)_3$ and Cr_2O_3 was observed on the surface of S13Cr at 90 °C, while the

59   observed corrosion product layers consist of $FeCr_2O_4$ and $FeCO_3$ at 200 °C. Han et al. [15] showed that

60   the structure of the passive film of 2205 DSS was composed of Cr_2O_3 inner layer, and a mixture of

61   Cr-rich and FeO outer layer at 30 °C –120 °C; while the passive film was degraded into an inner layer

62   of CrO_3 and $Cr(OH)_3$, and an outer layer containing iron(II, III) oxide and iron(III) oxide-hydroxide

63   when the temperature increased to 150 ℃. Recently, Willem et al., [17] found that 2205 DSS was

64   passivated, and the corrosion rate was low at 80°C in a CO_2-saturated geothermal brine, while the

65   passive film was damaged at the temperatures over 130°C. Mott-Schottky analysis and point defect

66   model (PDM) showed that the donor density and passivation current density of the passive film

67   increased with temperatures, reflecting high temperature decrease of the passive film stability [18,

68   19]. With the emergence of harsh and aggressive environments for geothermal exploitation, the

69   property of the passive film/corrosion product scales inevitably undergo changes that greatly affect

70   corrosion resistance of 2205 DSS. However, the previous research on 2205 DSS has mainly been

71   conducted at temperatures below 150℃. There is still a gap in the literature to investigate the

72   formation and evolution mechanism of the passive film or corrosion product scales on the 2205 DSS

73   surface under high-temperature ranges of 200-300°C.

74   Another considered parameter affecting the corrosion resistance of 2205 DSS, as well as the

75   formation of the corrosion products under arduous conditions is p_{CO2}. Geothermal production fluids

76   normally contain significant amounts of CO_2 in the range of 1–2.5% by weight [20]. CO_2 corrosion

77   ("sweet corrosion") has been discussed extensively by many authors in the oil and gas field under

78   low temperatures and low pressures [21-35]. High CO_2 pressure accelerates the corrosion processes

79   by lower pH and introducing significant amounts of substances (e.g., H_2CO_3, HCO_3^-). Yue et al. [23]

80   reported that the increase in p_{CO2} from 2.7 bar to 28.5 bar, resulting in a decrease in the

81   thermodynamic stability of spinel nano polycrystalline products of $FeCr_2O_4$, the corrosion scales

82   were mainly $FeCO_3$ crystals on 13Cr surface at high p_{CO2} at 200°C. Lu et al [37] studied the corrosion

83   behavior of S13Cr and found that the increase in p_{CO2}, resulting in accelerating the pitting corrosion

84   and repassivation ability became worse. However, the effect of p_{CO2} on the corrosion behaviour of

85   2205 DSS and related studies are rare.

86   Little evidence has been reported in the literature relating to the corrosion behaviour of 2205 DSS

87   immersed in the geothermal conditions (where temperatures > 200 °C and p_{CO2} > 20 bar). Studies

88   that refer to the evolution of the corrosion scales on 2205 DSS surface at 300°C regarding geothermal

environments are rare. Therefore, the current study is to address the knowledge gap for 2205 DSS exposed to CO_2-containing geothermal environments, to reveal the corrosion product evolution and corrosion behavior of 2205 DSS under temperature ranges from 100°C to 300°C. Characterization of the passive films and evolution of the corrosion scales were analyzed by various surface analysis techniques, including electron backscatter diffraction (EBSD), x-ray diffraction (XRD), scanning electron microscope (SEM), energy-dispersive X-ray spectroscopy (EDS), x-ray photoelectron spectroscopy (XPS), Raman spectroscopy and focused ion beam (FIB) and transmission electron microscopy (TEM). The constructed Pourbaix diagrams compared to the experimental results, both experimental results and Pourbaix diagrams were applied to determine the corrosion scale formation and reveal the fundamental mechanisms of 2205 DSS exposed to a geothermal environment.

2. Experimental

2.1 Material and methods

2205 DSS samples were machined into 23 mm x 13 mm x 5 mm. For the electrochemistry test, the sample was sealed in an HTHP resin and one surface of 0.785 cm^2 was exposed to the corrosive solution. Before both electrochemical and immersion tests, the samples were wet-ground up to 600 # using silicon carbide (SiC) paper, rinsed with DI-water, acetone, and dried by using a hot air gun. The samples were weighed (W_0) using an analytical balance with an accuracy of 10^{-5} g. Two samples were immersed in a 625 mL CO_2-saturated solution by using a 1 L autoclave, the volume of solution to the exposed surface ratio is 33 ml/cm^2. The chemical compositions of 2205 DSS and geothermal solutions are shown in Table 1 and Table 2.

Table 1 2205 DSS composition (wt. %)

CRA	Mn	Ni	Mo	Si	N	S	P	Cr	C	Fe
2205 DDS	1.2	5.6	3.08	0.6	0.17	0.002	0.02	22.5	0.02	Bal.

Table 2. Geothermal solution composition

Composition	Na$^+$	K$^+$	Ca^{2+}	Cl$^-$	HCO$_3^-$	SO$_4^{2-}$
Content (mg / L)	100300	250	510	155000	1635	335

Figure S1 shows the immersion and electrochemical setup within the autoclave. Two samples in the autoclave were fixed to a non-conductive sample holder which was made of polyether ether ketone (PEEK) for the immersion test. The solution used in tests was de-aerated by continuously purging with CO_2 for a minimum of 12 h. Once the sample was placed in the autoclave and sealed, all the lines and autoclave were purged by high-pressure CO_2 to remove the remaining O_2 within the system, and then prepared solution was transferred into the autoclave via a booster pump, followed by pressurizing the autoclave to a specific p_{CO2} at 25°C and heating to the required testing temperature. The test conditions for this study are provided in Table 3. The predicted initial pH for the test solution was given in Table 3 at various temperatures and p_{CO2} via OLI software [37].

Table 3. Test matrix for corrosion tests under different conditions

Temp (°C)	CO$_2$ pressure at 25°C (bar)	pH	p_{CO2}	Total pressure (bar)	Duration (days)
150	1	5.55	9.8	14.5	10
	20	5.26	27.4	33.4	
300	1	6.85	8.4	75	2
					5
					10
	20	5.84	32.8	108	2
					5
					10

The samples were removed from the autoclaves after the experiment and rinsed with Di-water, followed by drying thoroughly with a hot air gun. For the removal of the corrosion scales, the procedures were followed by ASTM G1-03 standard (Designation C.3.1) [38] and weighed again to obtain the final weight (W_2). Eq. (1) was used to calculate the corrosion rate (C_R) in mm/year:

$$C_R = \frac{87600 \ (W_0 - W_2)}{t\rho A} \qquad (1)$$

where t is the immersion time, h, ρ is steel density, g/cm^3, A is exposed surface area in cm^2.

2.2 Electrochemical measurements

For the electrochemical measurements, the autoclave was coupled with a standard 3-electrode, a platinum counter electrode, a working electrode of 2205 DSS, and a 0.1 M KCl Ag/AgCl reference electrode as shown in Figure S1b. For all measured potentials within this study, the electrode potential vs standard hydrogen electrode (SHE), known as E_{SHE} was calculated via equation (2) [39]:

$$E_{\text{SHE}} = E_{\text{obs}} + 0.2866 - 0.001(T - T_0) + 1.745 \times 10^{-7}(T - T_0)^2 \qquad (2)$$
$$- 3.03 \times 10^{-9}(T - T_0)^3$$

where E_{obs} is the measured potential vs the Ag/AgCl reference electrode, T is the temperature and T_0 is 25℃.

Electrochemical performance of 2205 DSS at a wide temperature range between 100°C and 300°C in a geothermal environment was performed via cyclic polarization (CP) tests. The scan started from 150 mV below open circle potential (OCP), the scan rate was 1 mV/s, and the reversed current density was 5 mA/cm^2 for temperature ranges between 100 ℃ and 270 ℃, 15 mA/cm^2 was set for 300 ℃. The repassivation potential (E_{rp}) was measured by CP measurements for localized corrosion susceptibility according to ASTM G61 [40]. The pitting potential (E_p) was also determined by CP curves.

2.3 Surface analysis

A detailed surface characterisation including SEM, XRD, Raman spectrometry, XPS, FIBs/TEM was used to identify the surface morphology, chemical composition, and structure of the passive film or corrosion products formed on the 2205 DSS surface.

3. Results

3.1 Microstructure characterisation

We firstly used EBSD to examine the microstructure of 2205 DSS and the results are provided in Figure 1. The phase distribution of 2205 DSS is shown in Figure 1a, the blue area (48%) was the ferrite phase, and the red area (52%) represented the austenite phase. It shows that the island-like austenite phase was embedded in the continuous ferrite phase. Figure 1b shows a grain orientation map of the examined areas, indicating the grains with an average grain size of 4.0 µm of diverse orientations. The results agree with the observations by Tian [41] and Dong [42].
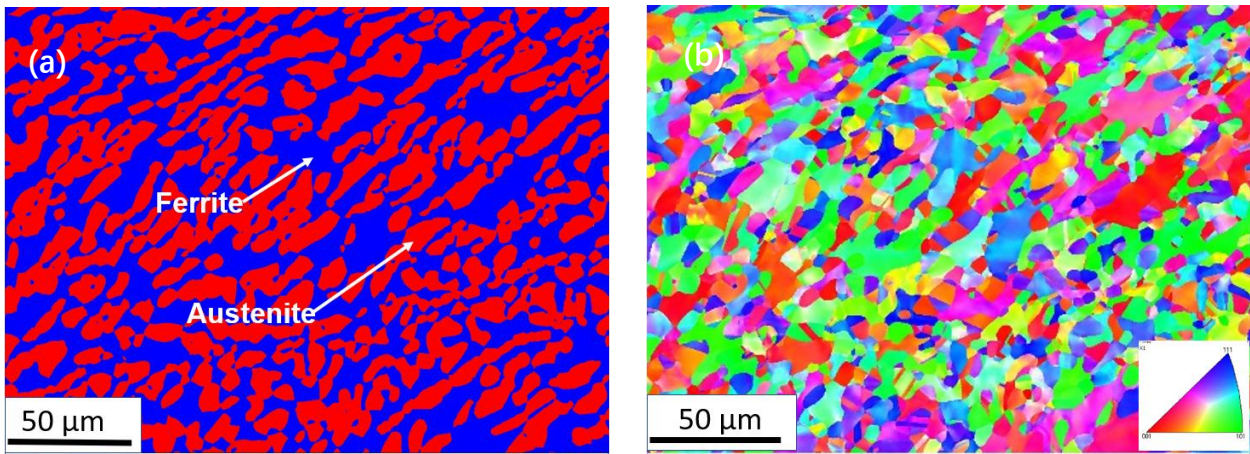
Figure 1. Microstructure of 2205 DSS: (a) phase distribution, (b) inverse pole figure (IPF) map of the grain orientation.

3.2 Electrochemical properties

Figure 2 displays the CP curves of 2205 DSS samples immersed in the CO_2-saturated geothermal solution at the temperature ranges between 100 °C and 300 °C, the overall analysis is summarised in Table 4. The results show that 2205 DSS exhibited obvious passivation ability at 100°C. From 100°C to 300°C, the corrosion potentials (E_{corr}) decreased from -414 mV to -730 mV and the passive current densities (i_p) increased from 48.5 ± 13.9 μA/cm^2 to 5158.3 ± 434.0 μA/cm^2 respectively. E_p decreased 160 mV to the negative direction with the temperatures increased from 100°C to 150°C. It is interesting to note that there was a significant increase in i_p as the temperatures rose from 150°C to 210°C or from 240°C to 300°C. Moreover, E_p shifted toward a negative direction with temperatures, suggesting that the deterioration in the corrosion resistance performance and the passive films were easier to breakdown at high temperatures. Another important feature that can be drawn from the CP curves is the repassivation potential decreased with the increase in temperatures, the passive film was failed to re-passivated at 300°C. The results indicate a tendency of the decreasing corrosion resistance of 2205 DSS at various geothermal temperatures, 100°C > 150°C >210°C > 240°C >300°C.
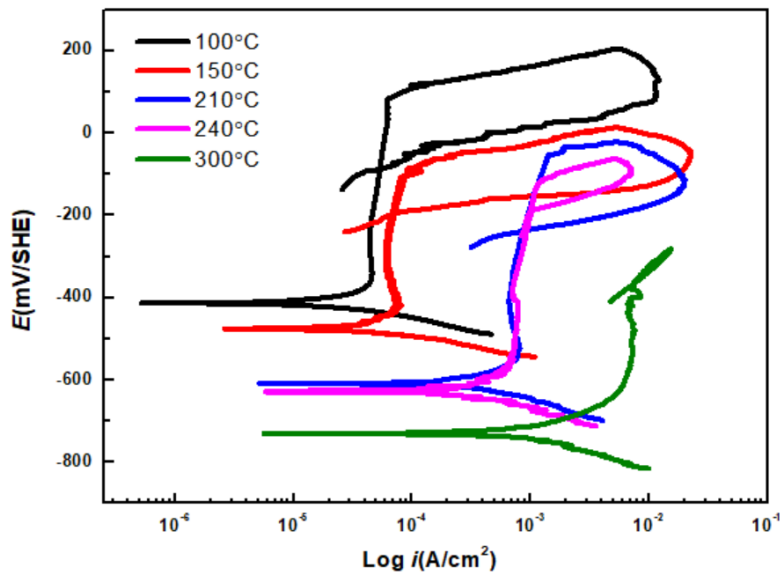
Figure 2 Cyclic polarization curves for 2205 DSS in geothermal solution at different temperatures

Table 4 The measured data for 2205 DSS at various temperatures

Temperature (°C)	E_{corr} (mV$_{SHE}$)	i_p (μA/cm^2)	E_p (mV$_{SHE}$)	E_{rp} (mV$_{SHE}$)
100	-414	48.5 ± 13.9	74	-87
150	-479	57.7 ± 10.3	102	-212
210	-608	785.2 ± 262.9	-57	-232
240	-628	756.7 ± 195.6	-116	-187
300	-730	5158.3 ± 434.0	-365	-365

3.3 Corrosion measurements of 2205 DSS immersed in the CO$_2$-saturated solution at various temperatures.

3.3.1 Characterisation of the passive films at 150°C

Figure 3 shows the macroscopic pictures of 2205 DSS before and after 10 days of exposure at 150°C and different p_{CO2}. The sample surfaces were still shining after 10 days of exposure. The pictures suggest that 2205 DSS was in a passive state at 150 °C and the corrosion rate from mass loss can be negligible under the test conditions here.
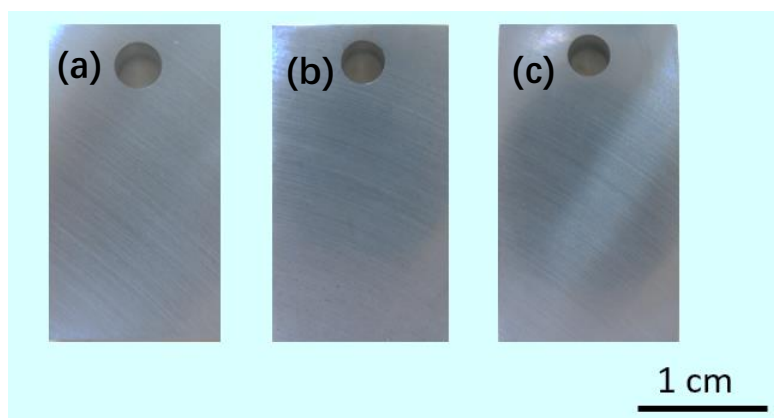
Figure S2 shows SEM images and conducting local Raman measurements from the sample surface. It is clear to see that the polishing marks were still visible for both p_{CO2} after 10 days of exposure. Raman measurements cannot detect any peaks for the corrosion products due to the thickness of the passive film was too thin.

**Figure 3 Macroscopic pictures of 2205 DSS in 150°C conditions for 10 days at different p_{CO_2} (a) before the test, (b) 9.8 bar, (c) 27.4 bar**

To complement the Raman spectroscopy analysis, confirming the passive film was still existence on 2205 DSS surface after exposure to the solution for 10 days at 150°C. Figure 4 shows high-angle annular dark-field (HAADF) images and EDS mapping via TEM measurement. The results indicate that a thin passive film with a thickness of approximately 20 nm was observed. High levels of Cr, O contents, and a trace amount of Ni contents were detected within the nano-size passive film via EDS mapping. Figure 4b shows the high-resolution transmission electron microscope (HRTEM) image of the passive film, indicating that there were no lattice fringes, which suggests that this nano-size passive film at 150°C was amorphous. The high-resolution XPS spectrum of Cr 2p3/2 and O1s were collected on the passive film at 150°C and results are shown in Figures 5d and 5e. The peaks of Cr spectra were located at the positions of 576.7 eV and 577.3 eV, corresponding to Cr_2O_3 and $Cr(OH)_3$[43] respectively. The O1s spectra were split into two peaks, indicating as OH^-(531.6 eV) and O^{2-}(530.2 eV) within the passive film, respectively.
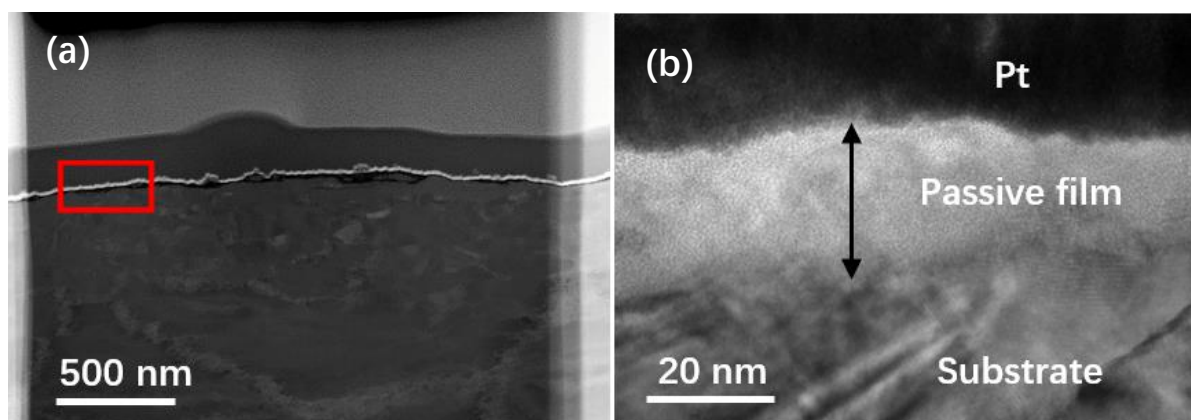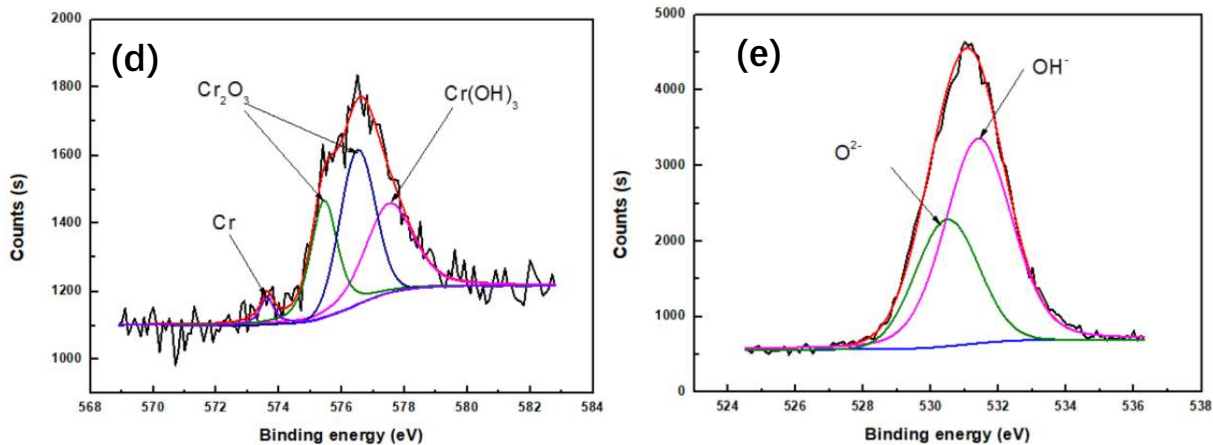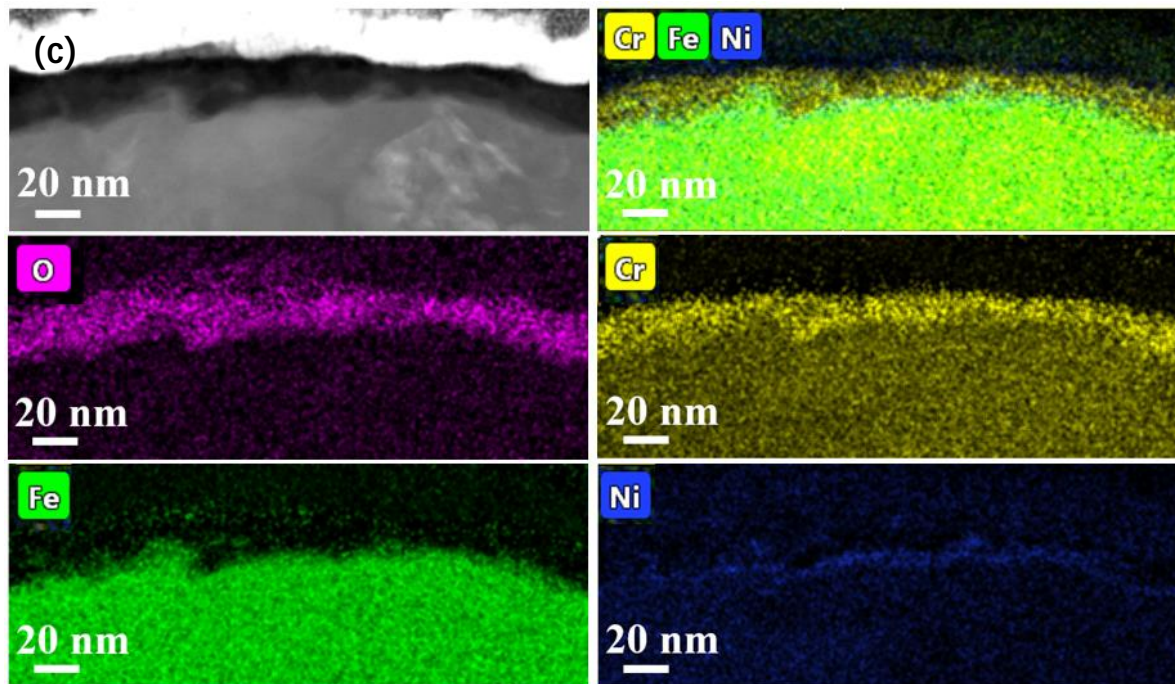
Figure 4. (a) FIB image, (b) HRTEM image, (c) EDS mapping, (d) XPS spectra of Cr 2p3/2, and (e) XPS spectra of O 1s of the passive film at 150 °C.

3.3.2 The immersion tests at 300°C

Increasing the temperature to 300 °C, the mass loss of 2205 DSS after immersing in the solution for 2 days, 5 days, and 10 days under both p_{CO2} of 8.4 bar and 32.8 bar is shown in Figure 5. The corrosion rates were low at both 8.4 bar and 32.8 bar p_{CO2} conditions, indicating that the corrosion rates were not affected by p_{CO2}, only a slight reduction in corrosion rate from 0.015 mm/y to 0.005 mm/y was measured with the increase of immersion time from 2 days to 10 days. The results suggest that 2205 DSS should provide good corrosion resistance under the current experimental conditions.

212
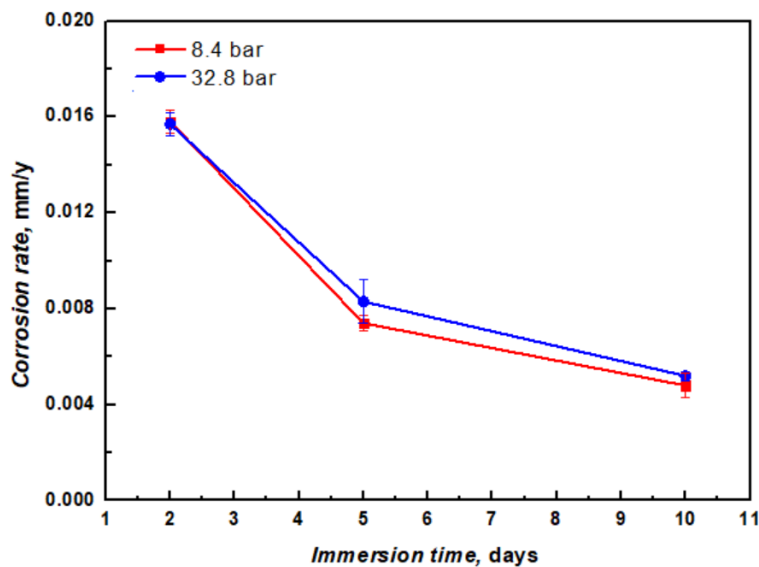
Figure 5 Corrosion rates of 2205 DSS immersed in the geothermal solution at 300°C and p_{CO2} of 8.4 bar and 32.8 bar

3.3.3 Characterisation of the corrosion product scales formed at 300 °C

Figure 6 shows the SEM morphology of corroded 2205 DSS surface after 2, 5 and 10 days of exposure at 300°C and p_{CO2} of 8.4 bar and 32.8 bar, respectively. For p_{CO2} of 8.4 bar condition, a clean surface with polished marks was observed after 2 days. After 5 days of exposure, discrete particles were randomly found on the surface via SEM (Figure 6c) and the particles increased in number and size with immersion time to 10 days as shown in Figure 6e.

Maintaining the temperature and the increase in the p_{CO2} up to 32.8 bar, small corrosion products appeared (Figure 6b) and were randomly distributed on the surface of 2205 DSS after 2 days of exposure. It can be seen that more corrosion products were observed on the surface of 2205 DSS after 5 days and 10 days of exposure at p_{CO2} of 32.8 bar compared to that of p_{CO2} of 8.4 bar, suggesting that p_{CO2} accelerated the formation of the corrosion products (Figure 6d and 6f).

Figure S3 illustrates the XRD patterns of the corrosion products formed on 2205 DSS surfaces at various immersion times at 8.4 bar and 32.8 bar p_{CO2}, respectively. The XRD pattern of a clean surface was also incorporated in the figure (black line) for comparison purposes. The results indicate two matrix structures, including austenite and ferrite phases in both p_{CO2} conditions. However, XRD measurements show that no crystalline signals were detected, suggesting that the corrosion products were too thin, or in amorphous nature and XRD cannot detect them.
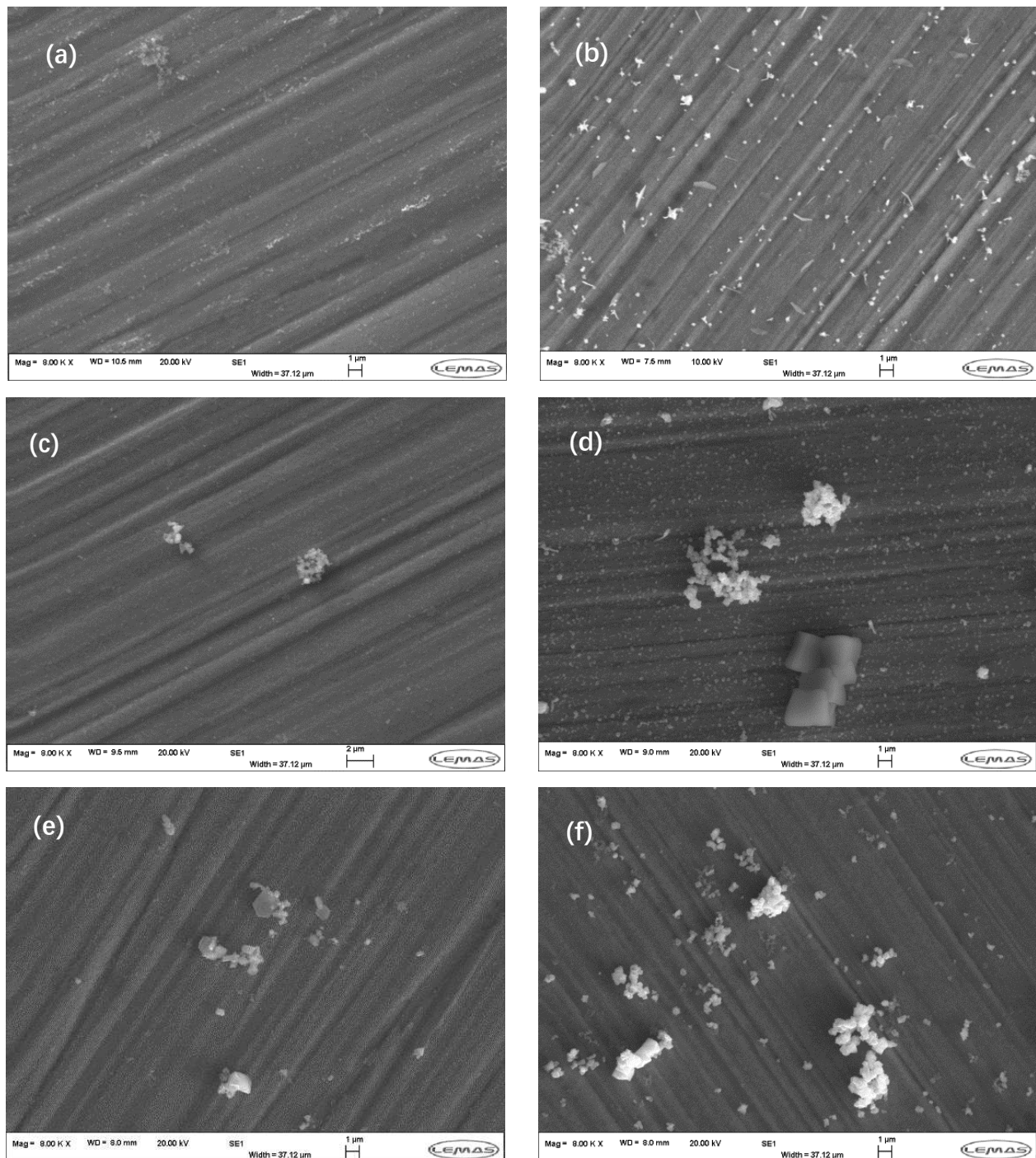
Figure 6 SEM images of the corrosion products at 8.4 bar p_{CO2} (after (a) 2 days, (c) 5 days, (e) 10 days) and 32.8 bar p_{CO2}(after (b) 2 days, (d) 5 days, (f) 10 days).

To confirm the existence of the corrosion products, Raman measurements in Figure 7 and Figure 8 are related to the local scans from the surface of 2205 DSS at p_{CO2} of 8.4 bar and 32.8 bar, respectively. The results confirmed that the same corrosion products were detected by Raman at both p_{CO2}, a strong Raman peak at 695 cm^{-1}, representing $FeCr_2O_4$ in both Figures. The increase in the immersion time to 5 days and 10 days, Raman results (in both p_{CO2} conditions) indicate that the weak peaks at 484 cm^{-1} and 726 cm^{-1} appeared, and representatives to $NiFe_2O_4$ as the outer scattered corrosion

products (A1 and B1 regions in both Figures). Refer to Figure 5, the results suggest that the $FeCr_2O_4$ inner layer was covered the entire surface of 2205 DSS, which was responsible to reduce the corrosion rate under these conditions.
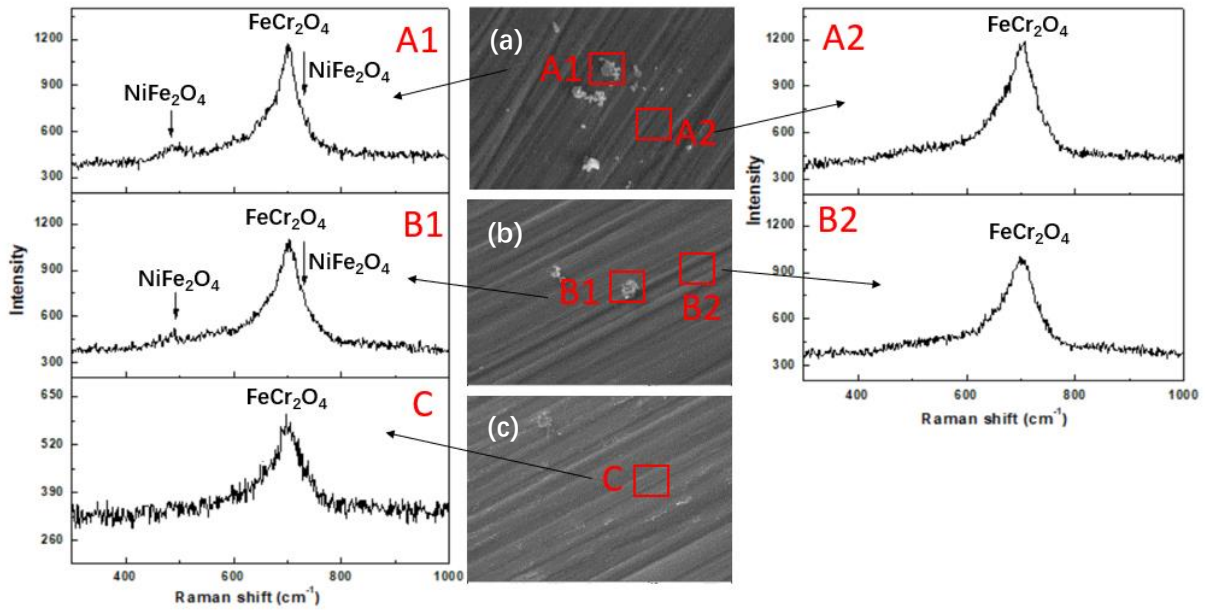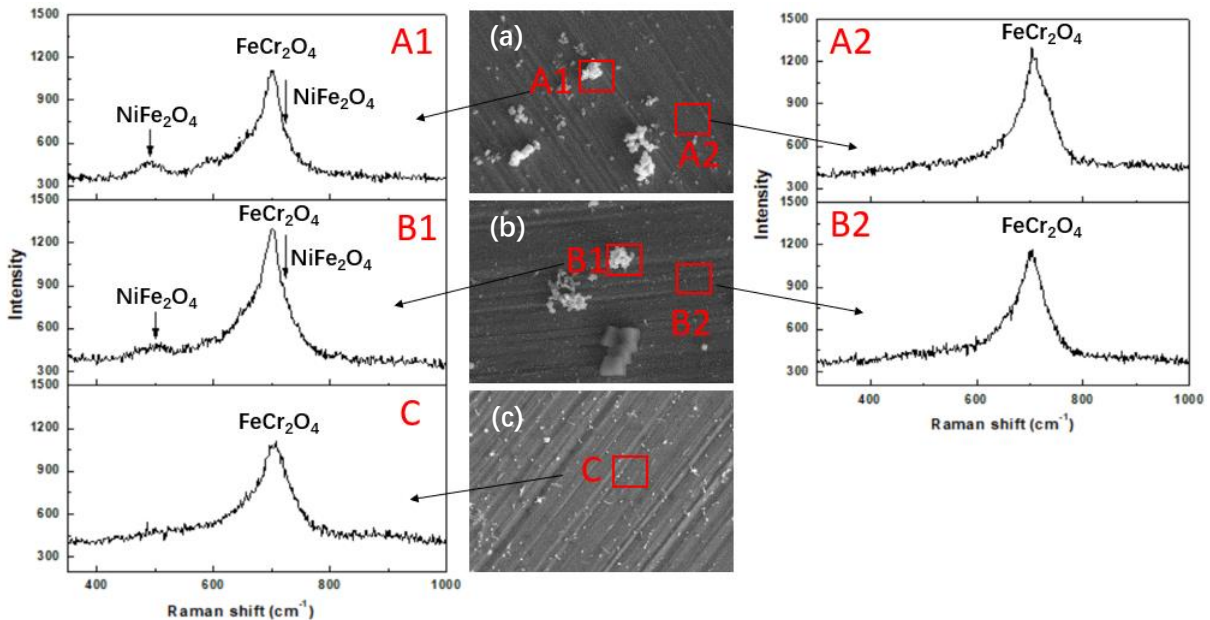

Figure 7. Raman spectra of 2205 DSS immersed in the geothermal water at 300°C and 8.4 bar p_{CO2} for (a) 10 days, (b) 5 days, and (c) 2 days.

**Figure 8. Raman spectra of 2205 DSS immersed in the geothermal water at 300°C and CO_2 p_{CO2} of 32.8 bar for (a) 10 days, (b) 5 days, and (c) 2 days**

The corrosion products were confirmed via XPS to supplement XRD and Raman results. Figure 9 illustrates the XPS spectra of Cr 2p3/2, Fe 2p3/2 and Ni 2p3/2 from 2205 DSS surface after 10 days

of exposure. XPS results indicate that the composition of the corrosion scales at 300°C was different from that of the passive film formed at 150°C. The Fe 2p3/2 spectra at 709 eV and 713.8 eV are presented in Figure 9a that demonstrates the presence of $FeCr_2O_4$, and the peak location at 710.5 eV corresponding to $NiFe_2O_4$. Meanwhile, the Cr 2p3/2 spectra were split into two peaks, corresponding to $FeCr_2O_4$ and CrOOH, respectively. Simultaneously, the fitting curve of Ni 2p3/2 was fitted well with the $NiFe_2O_4$ peak. Therefore, the corrosion products at 300 °C were mainly CrOOH, $FeCr_2O_4$ and $NiFe_2O_4$.
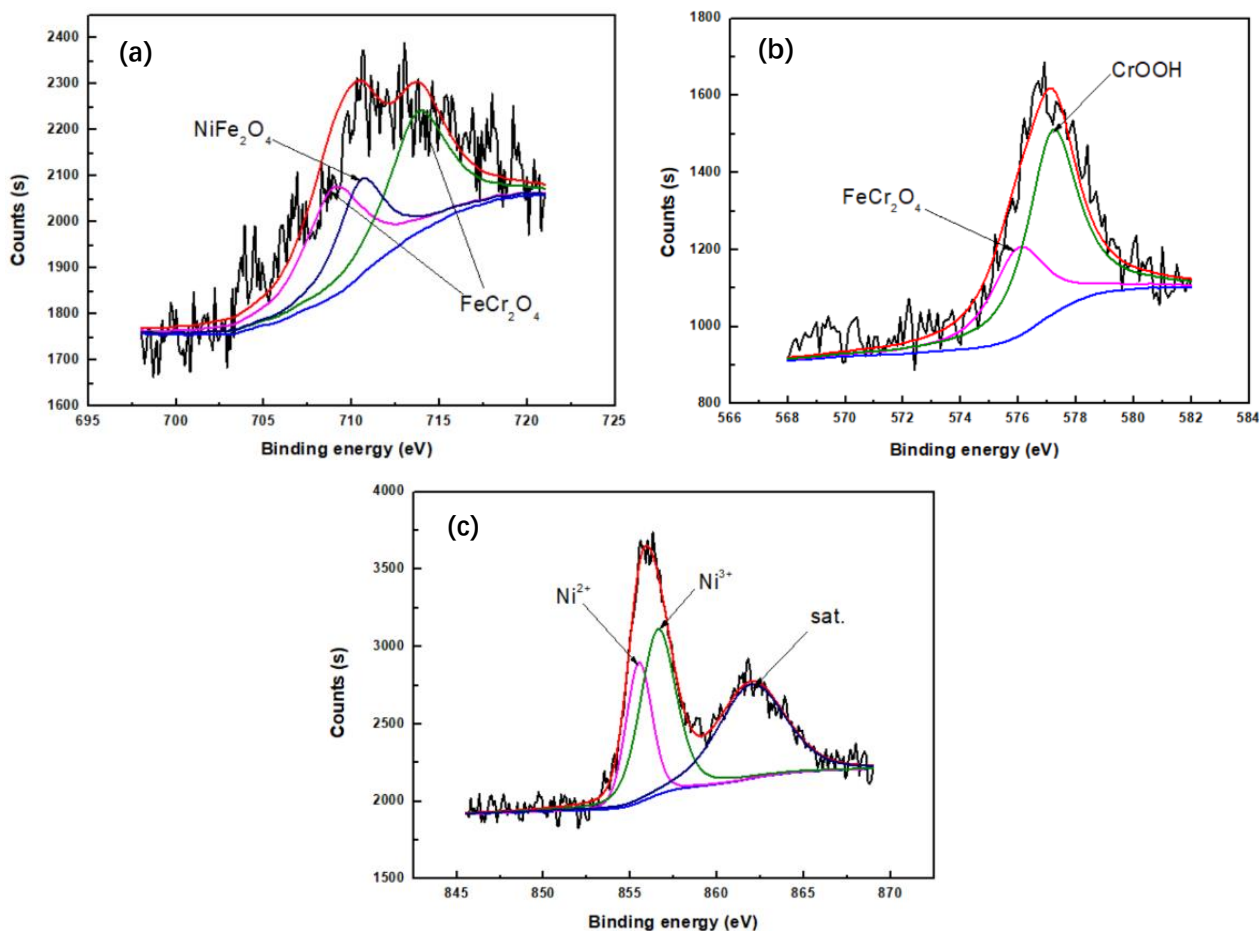

Figure 9. XPS spectra of the corrosion scales at 300°C and 32.8 bar CO_2 p_{CO2}, (a) Fe 2p3/2 peaks, (b) Cr 2p3/2 peaks, (c) Ni 2p3/2 peaks

To further characterisation of the corrosion product scales formed on the surface of 2205 DSS at 300°C and distinguish the essential structure and elemental composition difference from the films at 150°C, both FIB-SEM and TEM were used. Figure 10a shows an SEM image of the selected area of the corrosion products for FIB sample. Figure 10b indicates the cross-sectional FIBs sample from the selected region in Figure 10a. It is interesting to note that the outer crystals were composed of several small crystals and the overall thickness of the outer oxide crystals was 1 μm. Figure 10b

shows that a thin interface layer between the outer corrosion products and the steel substrate was observed, indicating a varied thickness between 100 nm and 200 nm.

High magnification TEM images in Figure 10(c-e) show the electron diffraction pattern of the corrosion products from region A in Figure 10b. Figures 10d, 10e and 10f illustrate the local electron diffraction patterns from different scanned areas from Figure 10c. The outer layers were verified as $NiFe_2O_4$ crystals (Figure 10d) and nano-polycrystalline $FeCr_2O_4$ (Figure 10e) respectively. The uniform inner layer as shown in Figure 10f was confirmed as nano-polycrystalline $FeCr_2O_4$ and the amorphous diffraction rings were detected which indicates amorphous structures coexist within the crystalline products, this amorphous layer was identified as the undamaged Cr_2O_3, similar observation of undamaged passive film on S13Cr immersed in the high-temperature CO_2-containing environment has been reported by Yue et al. [44]
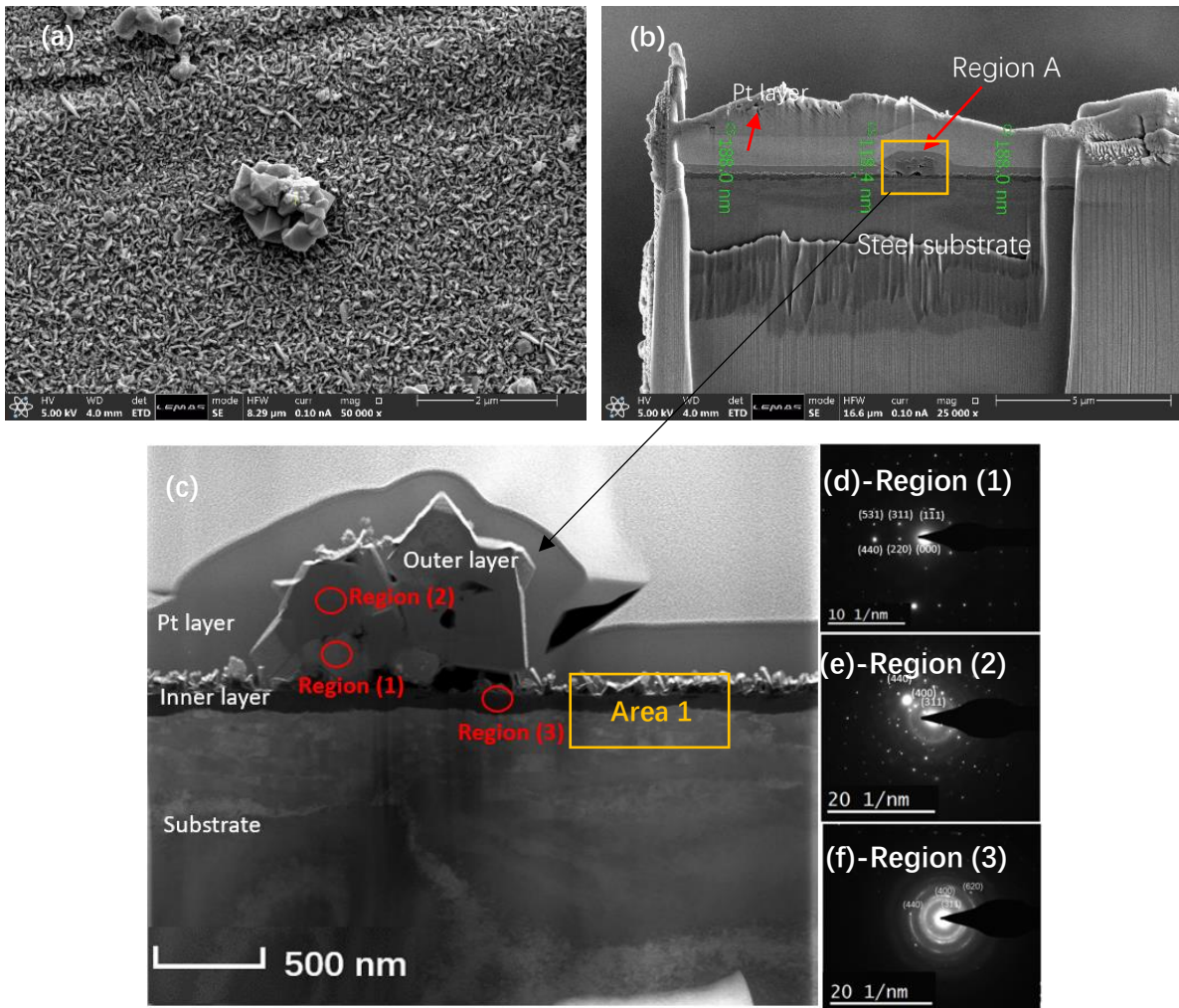
Figure 10. SEM image of the analysis region at 300°C and 32.8 bar p_{CO2} after 10 days, (a) before Pt deposition region, (b) produced FIB sample for TEM preparation, TEM image (c) and the electron

The corrosion products were further analysed via the EDS line scans to indicate the distribution of the elemental composition. Figure 11 indicates that the corrosion product scales were comprised of two layers, both inner and outer corrosion layers were containing Fe, Ni, Cr, and O. However, the concentration of Cr within the inner layer was higher than the outer layer. The results suggest that the $FeCr_2O_4$ inner layer plays a vital role in the corrosion resistance of 2205 DSS via restricting the passway of corrosive ions. Besides, high Ni was detected within the outer crystal, which agrees with the TEM and Raman measurements that the outer crystal was mainly $NiFe_2O_4$. It also can be noted that the Cr content in some areas was relatively high, suggesting $FeCr_2O_4$ was coexisted with $NiFe_2O_4$.
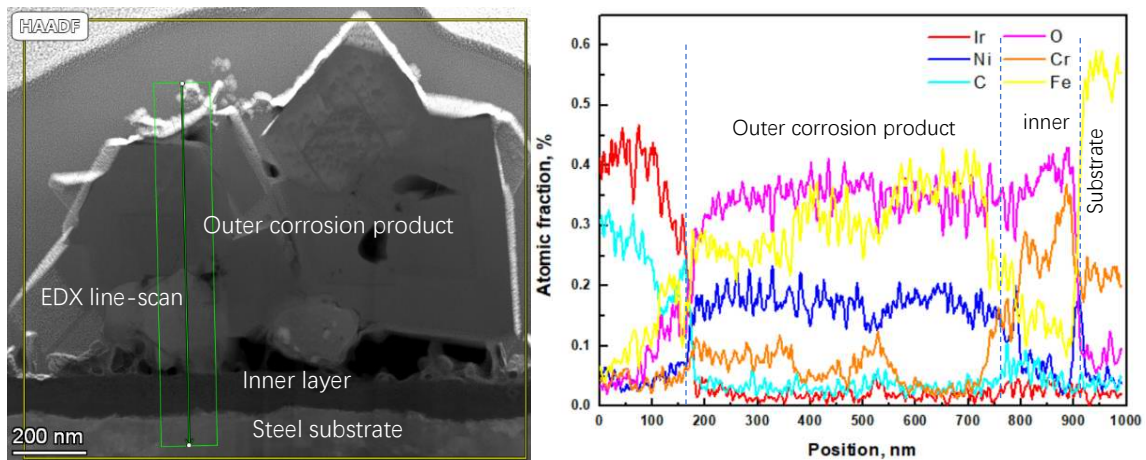
Figure 11. Line scans across the whole corrosion product layers at 300°C and 32.8 bar p_{CO2}.

## 4. Discussion

4.1 The passive film forms at 150°C

Figure 12 indicates the constructing Pourbaix diagram at 150°C for 2205-CO_2-Cl^--H_2O system, considering the initial pH of 5.26 and corrosion potential of -0.48 V/SHE at 150°C, the presence of Cr_2O_3 was calculated as the thermodynamically stable product with the coexisting products of $Cr(OH)^{2+}$ ions in the aqueous phase. The development and dissolution of the passive film in the initial period are through the following reactions [45, 46]:

$$2Cr + 3H_2O \leftrightarrow Cr_2O_3 + 6H^+ + 6e^- \qquad (3)$$

$$Cr_2O_3 + 3H_2O \leftrightarrow 2Cr(OH)^{2+} + 4OH^- \qquad (4)$$
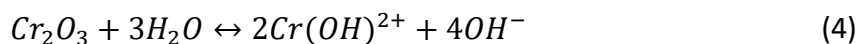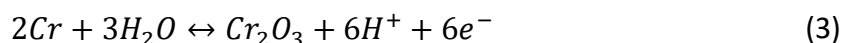
Bischoff et al., [48] performed the in-situ pH measurement on the 316L SS surface, they indicated that the pH of the bulk solution was unchanged, while the near-surface pH increased significantly with

the immersion times when the material was in a passive state. According to the constructing

Pourbaix diagrams, the presence of Cr(OH)$_3$ was considered as the thermodynamically stable

coexistence product in the passive film, which acted as a barrier for dissolution and suppressed the

corrosion. The transformation between Cr$_2$O$_3$ and Cr(OH)$_3$ is shown in equation (5); this reaction

replaced the dissolution of Cr$_2$O$_3$ into ions and thickened the passive film by forming a Cr(OH)$_3$ outer

layer, the results agree with XPS and TEM analyses of the passivation film at 150°C as shown in Figure

4.

$$Cr_2O_3 + 3H_2O \leftrightarrow 2Cr(OH)_3 \tag{5}$$
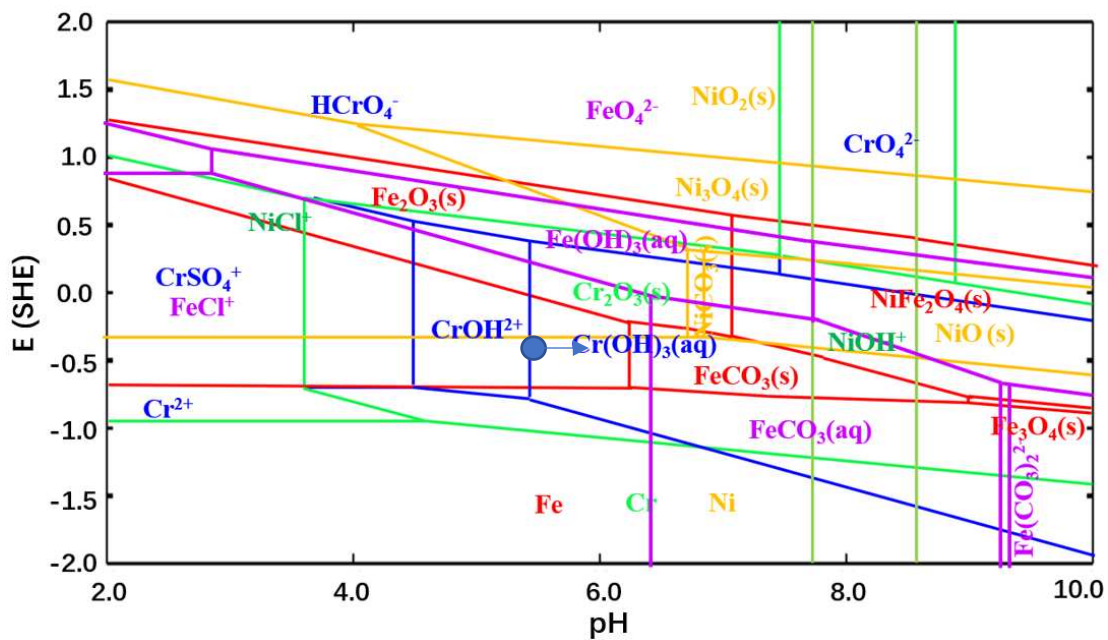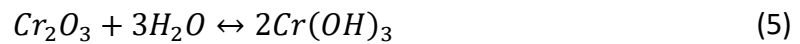
Figure 12. Pourbaix diagrams of 2205 DSS immersed in geothermal solution at 150°C and 27.4

bar p_{CO2}

Figures 4 indicates that a double-layered passive film was observed at 150°C. The inner passive layer

formed via direct oxidation of the base metal, and the formation of the outer passive layer was via

the precipitation and the transition from the coexistence oxide [7]. The growth of the inner layer

would be accompanied by the transformation (5) at the material interface between the inner/outer

layer and the following dissolution reactions at the outer layer/solution interface:

$$Cr(OH)_3 + 3H^+ \leftrightarrow Cr^{3+} + 3H_2O \tag{6}$$

$$2Cr(OH)_3 + 3H_2CO_3 \leftrightarrow 2Cr^{3+} + 6H_2O + 3CO_3^{2-} \tag{7}$$
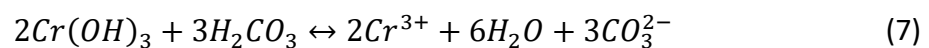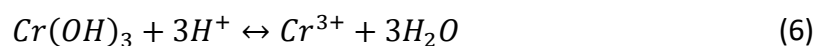
The transformation of the outer Cr(OH)$_3$ passive layer suggests that the pH at least should be 5.44

at the material interface. The dissolution equilibrium via reactions (6) and (7) will further release
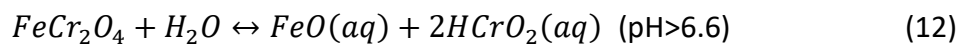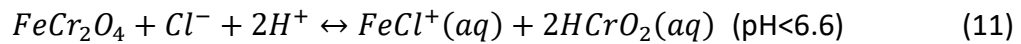
318   alkalinity and increase the pH value.

4.2 Corrosion mechanism at 300°C

320   For 2205 DSS exposed to 300 °C, the conducting Pourbaix diagram for 2205-CO_2-Cl⁻-H_2O system (OCP

321   potential of -0.73 V/SHE and solution pH of 5.84 was considered) is shown in Figure 13. The

322   thermodynamic stable corrosion products at this temperature are mainly comprised of $FeCr_2O_4$ and

323   CrOOH. This result is consistent with TEM and XPS results as shown in Figure 9 and Figure 10, where

324   the inner layers were mainly nano-polycrystalline $FeCr_2O_4$ and CrOOH.

325   The presence of Cr in 2205 DSS oxidized to form $CrOOH$ and followed by the formation of $FeCr_2O_4$,

326   as shown in reactions (8)-(9):

$$Cr + 2H_2O \rightarrow CrOOH + 3H^+ + 3e^- \tag{8}$$

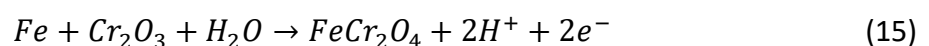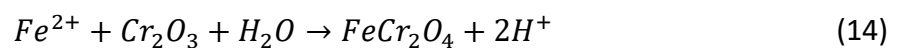$$Fe + 2CrOOH \rightarrow FeCr_2O_4 + 2H^+ + 2e^- \tag{9}$$
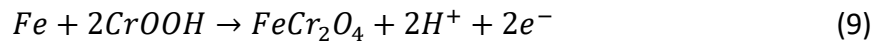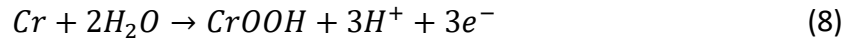
327   The formation of the inner layer composed of $CrOOH$ and $FeCr_2O_4$ turning the 2205 DSS into a

328   passivation state and maintained equilibrium with the coexisting products in the aqueous phase

329   through the following reaction:

$$CrOOH \leftrightarrow HCrO_2(aq) \tag{10}$$

$$FeCr_2O_4 + Cl^- + 2H^+ \leftrightarrow FeCl^+(aq) + 2HCrO_2(aq) \quad \text{(pH<6.6)} \tag{11}$$

$$FeCr_2O_4 + H_2O \leftrightarrow FeO(aq) + 2HCrO_2(aq) \quad \text{(pH>6.6)} \tag{12}$$

330   It is noted that $FeCr_2O_4$ yields a relatively narrow thermodynamically stable region compared with

331   that of $CrOOH$. Local acidification to the pH below 4.53 results in the degradation of the solid

332     $FeCr_2O_4$ and the release of iron ions:

$$FeCr_2O_4 + Cl^- + 2H^+ \rightarrow FeCl^+ + CrOOH \tag{13}$$
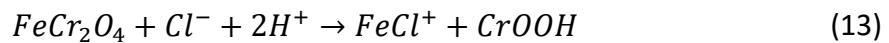
333   As the temperature rose to 300°C, Cr_2O_3 was no longer thermodynamically stable. The presence of

334   Cr_2O_3 as shown in XPS measurement could be from the residual pre-existing passive film [16], the

335   presence of Cr_2O_3 was locally damaged and transformed into corrosion product scales at high

336   temperature via the following reactions:

$$Fe^{2+} + Cr_2O_3 + H_2O \rightarrow FeCr_2O_4 + 2H^+ \tag{14}$$

$$Fe + Cr_2O_3 + H_2O \rightarrow FeCr_2O_4 + 2H^+ + 2e^- \tag{15}$$

$$Cr_2O_3 + H_2O \rightarrow 2CrOOH \tag{16}$$

$$Cr_2O_3 + H_2O \rightarrow 2HCrO_2(aq) \tag{17}$$
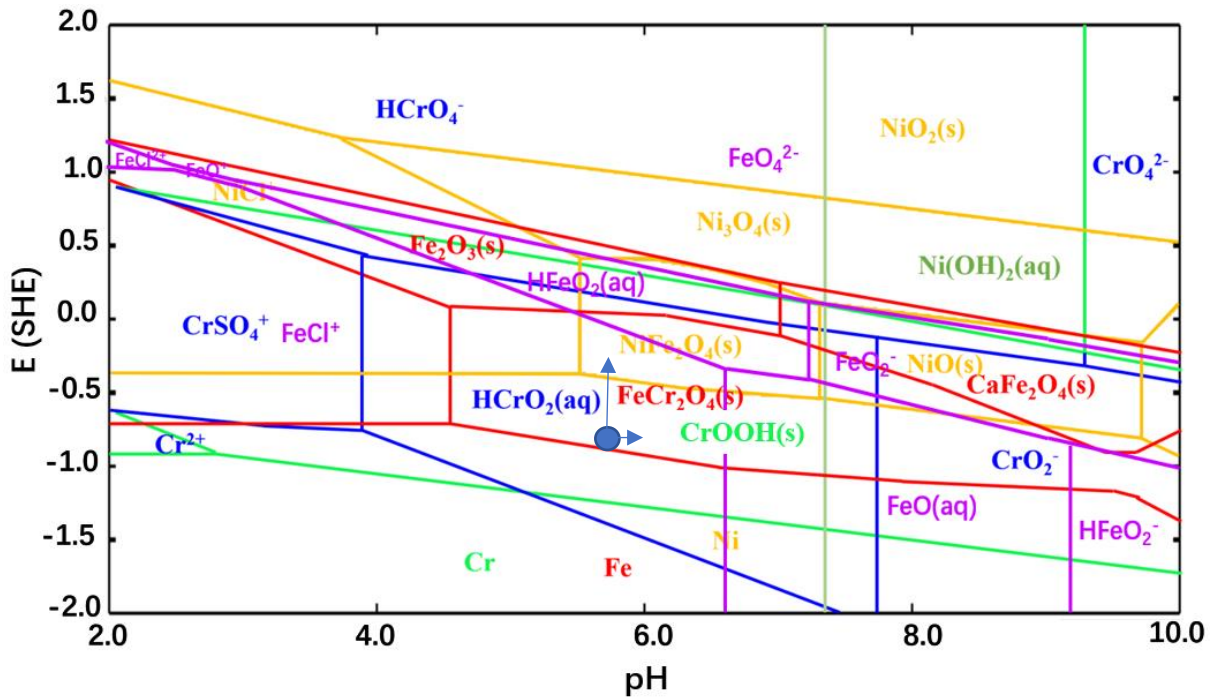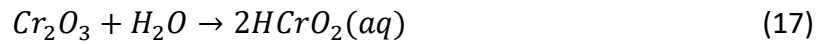
Figure 13. Pourbaix diagrams of 2205 DSS immersed in geothermal solution at 300°C and 32.8 bar p_{CO2}.

A wide thermodynamically stable region for Ni^0 was observed in comparison to that for Fe and Cr in the substrate. The enrichment of Ni beneath the film was attributed to the preferential dissolution of Fe and Cr [48] and the slow diffusion rate of Ni [49, 5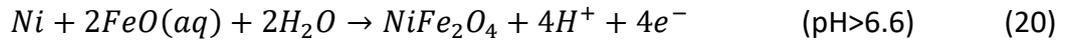0]. The Ni-rich layer at the material interface can play a key role in the development of the corrosion layers and slowing down the consumption of Cr^{3+} and Fe^{2+} [16]. The depressed nucleation of $FeCr_2O_4$ resulted in higher kinetics of crystallization [48]. The formation of an enriched Ni layer hindered the dissolution of Cr^{3+} and Fe^{2+} ions and retarded the evolution of the $FeCr_2O_4$ layer. Once the growth rate of $FeCr_2O_4$ was lower than the crystallization rate, the film with nanocrystals features formed on the surface, as confirmed in Figure 10.

The results at 300°C and p_{CO2} of 8.4 bar and 32.8 bar confirmed the presence of $NiFe_2O_4$ crystals that were relative to the localised surface chemistry at the outer surface, in which the corrosion potential should be up to -0.35 V as suggested in the constructing Pourbaix diagram in Figure 13. During the penetration of Fe/Cr oxidation, the remained Ni^0 at the outer interface acted as a nucleation site and reacted with the concentrated Fe^{2+} ions to form $NiFe_2O_4$ according to reactions (18-20) [51-53].

$$Ni + 2FeCr_2O_4 + 4H_2O \rightarrow NiFe_2O_4 + 4HCrO_2(aq) + 4H^+ + 4e^- \tag{18}$$

$$Ni + 2FeCl^+(aq) + 4H_2O \rightarrow NiFe_2O_4 + 2Cl^- + 8H^+ + 4e^- \quad (pH<6.6) \tag{19}$$

$$Ni + 2FeO(aq) + 2H_2O \rightarrow NiFe_2O_4 + 4H^+ + 4e^- \quad (pH>6.6) \tag{20}$$

356 As the immersion time prolongs, the growth of $NiFe_2O_4$ particles increased in both size and number
357 as shown in Figure 6.

358 Figure 14 illustrates the elemental distributions for the inner corrosion layers. It is noted that Cr was
359 non-uniformly distributed, and an inner Cr-enrichment layer was observed near the substrate due
360 to the preferential formation of CrOOH. The formation of CrOOH blocked the active dissolution and
361 raised the corrosion potential to the thermodynamically stable region for $FeCr_2O_4$. The formation of
362 $FeCr_2O_4$ consumed CrOOH via reaction (9) and resulted in the formation of a Fe-rich layer above the
363 Cr-rich layer. A Ni-rich layer at the interface between the inner layer and substrate was observed
364 with a thickness of 20 nm and can be identified as a crucial barrier against corrosion due to its
365 continuous coverage of the entire surface. The characterisation of the inner layers was mainly
366 comprised of Ni-rich layer, CrOOH, and $FeCr_2O_4$, suggesting that these corrosion products verified
367 the effective block against ion diffusion and lower the corrosion rate.
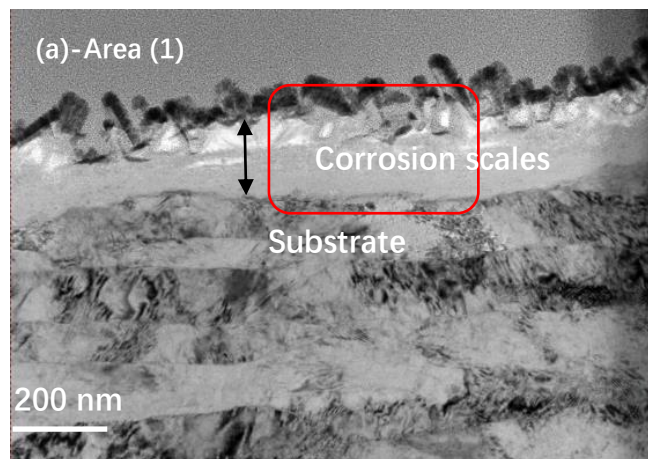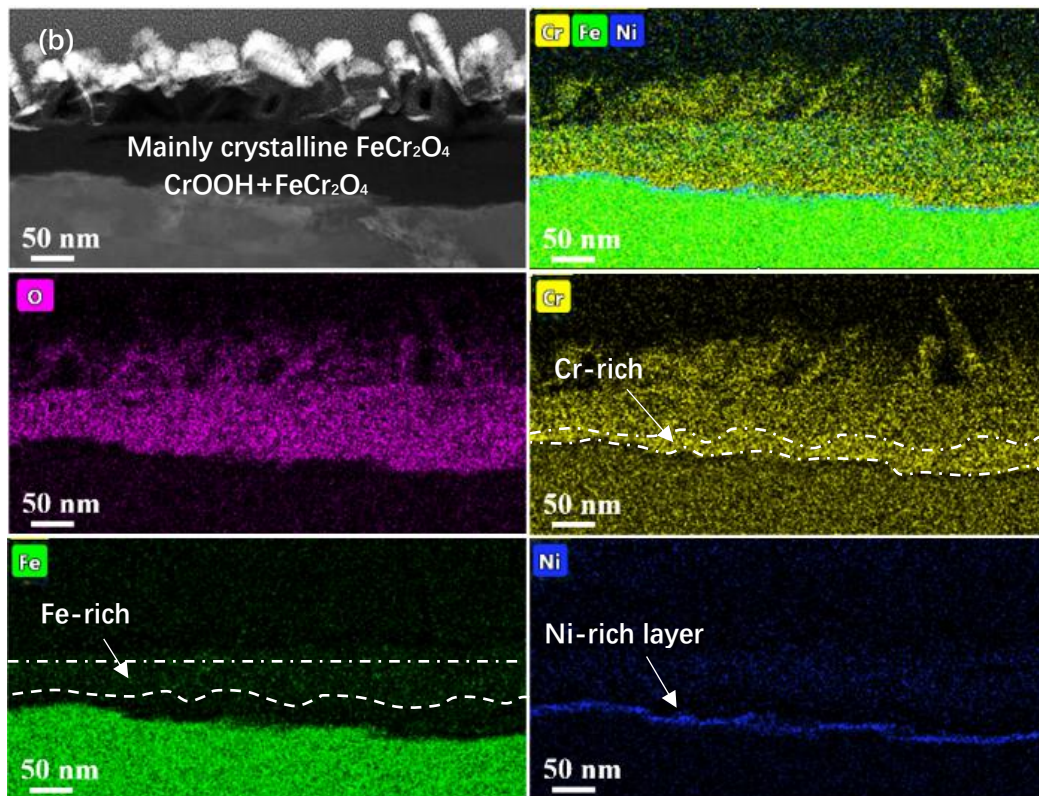
Figure 14. (a) HRTEM image on Area (1) in Figure 17 and (b) element distributions of the corrosion product inner layer via Super-X EDS mapping

4.3 The evolution and protectiveness of the corrosion scales at 300°C

Figure 15 represents a schematic diagram of the growth processes of the corrosion scales on the 2205 DSS surface at a 300°C geothermal environment. The formation of the corrosion products on the 2205 DSS surface at 300°C and 32.8 bar p_{CO2} including four stages: Stage I, the passive film was damaged locally, the initial passive film cannot stay in the thermodynamically stable state due to the high temperature of 300°C as well as the adsorption of chloride ions on the surface that led to its local destruction. Stage II, the growth of thermodynamically stable scale was comprised of $FeCr_2O_4$ and CrOOH, and the accumulation of the inner Ni-rich layer was attributed to the preferential dissolution of Fe and Cr and the slow diffusion rate of Ni. Stage III, the formation of the corrosion product layers restricted the anodic dissolution reactions and raised the corrosion potential to precipitation of the $NiFe_2O_4$ outer layer; Stage IV, the growth of the inner and outer corrosion products.
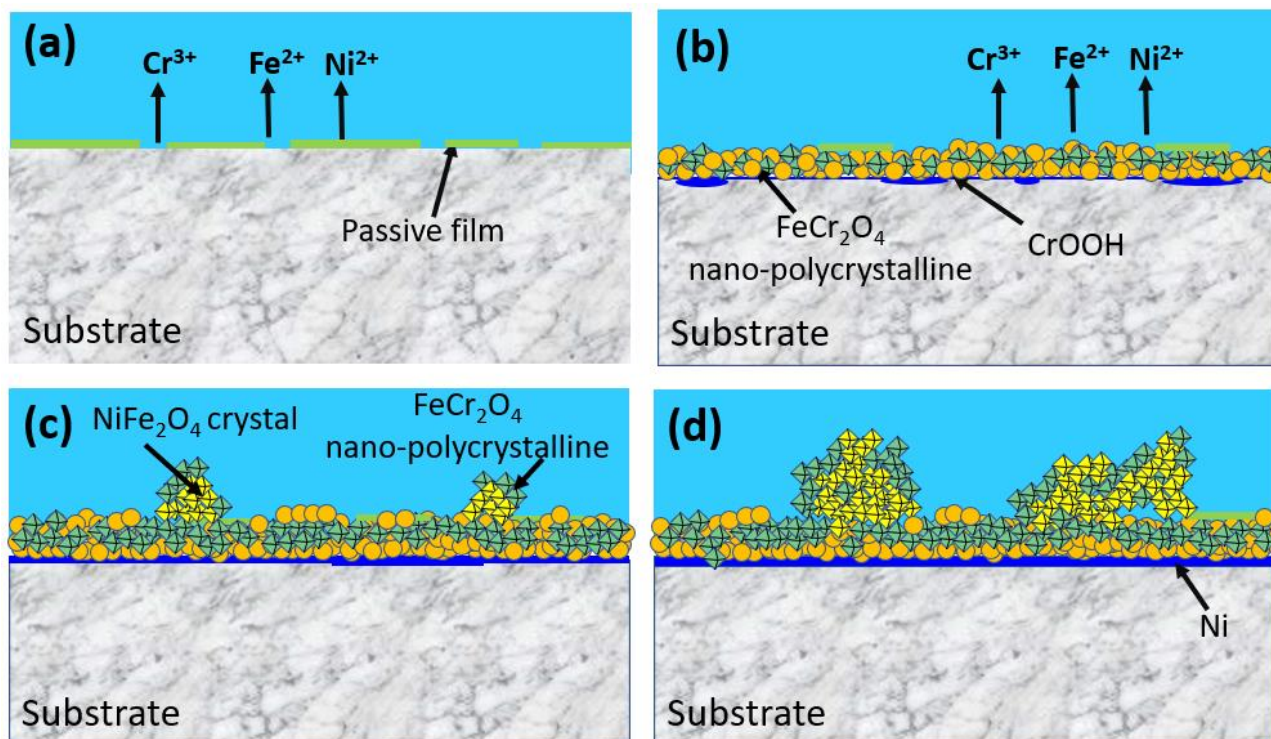
Figure 15. Schematics of the corrosion scale growth on 2205 DSS exposure to geothermal water at 300°C and 32.8 bar p_{CO2}

5. Conclusion

Surface characteristics of the passive film and the corrosion products were systematically investigated at various temperatures and p_{CO2}, the electrochemical behavior of 2205 DSS at various temperatures in a CO_2-saturated geothermal solution has also been reported:

1. A typical passive film was observed at 150°C compared with the growth of the corrosion products at 300 °C, indicating that 2205 DSS changed from passivation state to activation state as the temperatures increased from 150°C to 300°C.

2. At 150 °C, an amorphous layer mainly containing Cr_2O_3 and $Cr(OH)_3$ was detected. In the condition of 300 °C, a microscale layer containing nanocrystalline $FeCr_2O_4$, CrOOH, and $NiFe_2O_4$ was observed.

3. A Ni-rich inner layer was detected in both conditions of temperature at 150°C and 300°C via TEM measurements.

4. The results indicate that the increase in p_{CO2} has no significant influence on the corrosion rate of 2205 DSS at both 150°C and 300 °C.

5. The formation of the corrosion product scales on 2205 DSS at 300°C includes four stages: Stage I, the passive film was damaged locally. Stage II, the growth of thermodynamically stable products composed of $FeCr_2O_4$ and $CrOOH$ and the accumulation of the inner Ni-rich layer. Stage III, thickening the dominated $FeCr_2O_4$ and $CrOOH$ inner layers and following the precipitation of the crystalline $NiFe_2O_4$ and $FeCr_2O_4$; Stage IV, the growth of the inner and outer corrosion products.

6. Reference

[1] H. Shen, Current situation and development trend of geothermal energy development and utilization in China, Science and Technology Innovation, 14 (2019) 25-26.

[2] D. Zhou, Rich geothermal energy reserves in the world, Chinese and Foreign Energy, 21 (2016) 59.

[3] Y. Liu, Research on China 's Energy System Transformation and Renewable Energy Consumption Path, Lanzhou University, (2017).

[4] J. Nogara, S. J. Zarrouk, Corrosion in geothermal environment: Part 1: Fluids and their impact, Renewable & Sustainable Energy Reviews, 82(2017), 1333-1346.

[5] J. Nogara, S. J. Zarrouk, Corrosion in geothermal environment Part 2: Metals and alloys, Renewable & Sustainable Energy Reviews, (2018) S1364032117310444.

[6] A. Tomio, M. Sagara, T. Doi, H. Amaya, N. Otsuka, T. Kudo, Role of alloyed molybdenum on corrosion resistance of austenitic Ni-Cr-Mo-Fe alloys in H_2S-Clenvironments, Corrosion Science, 98(2015), 391-398.

[7] H. Amaya, T. Mori, K. Kondo, H. Hirata, M. Ueda, et al. Effect of chromium and molybedenum on

431   corrosion resistance of super 13Cr martenistic stainless steel in CO_2 environment Corrosion,

432   NACE International, Houston, Paper No. 98113, (1998).

433   [8] E. Okoro, A. M. Kurah, S. E. Sanni, A. Dosunmu, E. B. Ekeinde, Eng. Fail. Anal., 102 (2019) 160.

434   [9] P. Ernst, R. C. Newman, Pit growth studies in stainless steel foils. II. effect of temperature, chloride

435   concentration and sulphate addition, Corrosion Science, 44(2002), 943-954.

436   [10] E. Blasco-Tamarit, A. Igual-Munoz, J. G. Anton, D. Garcia-Garcia, Effect of temperature on the

437   corrosion resistance and pitting behaviour of Alloy 31 in LiBr solutions, Corrosion Science,

438   50(2008), 1848-1857.

439   [11] E. A. Abd El Meguid, A. A. Abd El Latif, Critical pitting temperature for type 254 SMO stainless

440   steel in chloride solutions, Corrosion Science, 49(2007), 263-275.

441   [12] Z. Szklarska-Smialowska, Pitting and Crevice Corrosion, NACE International, Houston(2005),

442   205-221.

443   [13] A. Keserovic, R. Bäßler, Suitability of UNS S31603 steel for geothermal brines in volcanic areas -

444   influence of different physicochemical conditions on its corrosion behavior, Geothermics,

445   53(2015), 479-487.

446   [14] X. P. Li , Y. Zhao , W. L. Qi , J. F. Xie, J. D. Wang, B. Liu, G. X. Zeng, T. Zhang, F. H. Wang, Effect of

447   extremely aggressive environment on the nature of corrosion scales of HP-13Cr stainless steel,

448   Applied Surface Science, 469(2019), 146-161.

449   [15] Z. Han, Effects of Temperature on Corrosion Behaviour of 2205 Duplex Stainless Steel in Carbon

450   Dioxide-Containing Environments, International journal of electrochemical science, (2020),

451   3627-3645.

452   [16] X. Q. Yue, L. Zhang, Y. Wang, S. S. Xu, C. Wang, M. X. Lu, A. Neville, Y. Hua, Evolution and

453   characterization of the film formed on super 13Cr stainless steel in CO2-saturated formation

454   water at high temperature, Corrosion Science, 163(2020), 108277.

455   [17] W. Faes, S. Lecompte, J. V. Bael, et al. Corrosion behaviour of different steel types in artificial

456   geothermal fluids, Geothermics, (2019), 82.

457   [18] C. Escrivà-Cerdán, E. Blasco-Tamarit, D. M. García-García, J. García-Antón, R. Akid, J. Walton,

458   Effect of temperature on passive film formation of UNS N08031 Cr-Ni alloy in phosphoric acid

459   contaminated with different aggressive anions, Electrochimica Acta, 111(2013), 552-561.

460   [19] A. Fattah-alhosseini, F. Soltani, F. Shirsalimi, B. Ezadi, N. Attarzadeh, The semiconducting

461   properties of passive films formed on AISI 316 L and AISI 321 stainless steels: a test of the point

462   defect model (PDM), Corrosion Science, 53(2011), 3186-3192.

463 [20] B. Wood, The utilization of geothermal fluids. In: Armstead HCH, editor. Geothermal energy:
464   review of research and development. UNESCO, (1973), [ISBN92-3-101063-8].

465 [21] A. Ikeda, S. Mukai, M. Ueda, Corrosion behavior of 9 to 25% Cr steels in wet CO_2 environments,
466   Corrosion 41 (1985) 185–192.

467 [22] X. Yue, M. Zhao, L. Zhang, H. Zhang, D. Li, M. Lu, Correlation between electrochemical properties
468   and stress corrosion cracking of super 13Cr under an HTHP CO_2 environment, RSC Adv. 8 (2018)
469   24679–24689.

470 [23] X Yue, Zhang L, Sun C, et al. A thermodynamic and kinetic study of the formation and evolution
471   of corrosion product scales on 13Cr stainless steel in a geothermal environment, Corrosion
472   science, 2020.

473 [24] J. Sun, W. Liu, W. Chang, Z. Zhang, Z. Li, W. Yu, M. Lu, Characteristics and formation mechanism
474   of CO_2 corrosion product film on low chromium X65 pipeline steel, Acta Metallurgica Sinica,
475   (2009), 86-92.

476 [25] G. Zhang, M. Lu, Y. Wu, Microscopic morphology and structural characteristics of CO_2 corrosion
477   product film, Chinese Journal of Materials Research, 19(2005), 537-548.

478 [26] K. Nose, H. Asahi, P. I. Nice, J. Martin, Corrosion Properties of 3% Cr Steels in Oil and Gas
479   Environments. Corrosion/2001, Paper No. 82. 2001.

480 [27] H. Zhang, Y. Zhao, Z. Jiang, Effects of temperature on the corrosion behavior of 13Cr martensitic
481   stainless steel during exposure to CO_2 and Cl environment, Materials Letters, 59(2005), 3370-
482   3374.

483 [28] T. Doi, T. Adachi, T. Kudo, N. Usuki, In situ investigation of CO_2 corrosion in Cr-containing steels
484   in CO_2-saturated salt solution at elevated temperatures and pressures, Corrosion Science,
485   177(2020), 108931.

486 [29] C. Li, Y. Zhang, B. Wang, J. Dai, Y. Chen, Research progress of CO_2 corrosion product film during
487   oil and gas development, Corrosion and Protection, 26(2005), 443-447.

488 [30] L. Wei, K. Gao, Q. Li, Corrosion of low alloy steel containing 0.5% chromium in supercritical CO_2-
489   saturated brine and water-saturated supercritical CO_2 environments, Applied Surface Science,
490   (2018).

491 [31] W. Liu, J. Dou, S. Lu, P. Zhang, Q. Zhao, Effect of silty sand in formation water on CO2 corrosion
492   behavior of carbon steel, Applied Surface Science, (2016).

493　[32] R.M. Moreira, C.V. Franco, C.J.B.M. Joia, S. Giordana, O.R. Mattos, The effects of temperature

494　　　and hydrodynamics on the CO_2 corrosion of 13Cr and 13Cr5Ni2Mo stainless steels in the

495　　　presence of free acetic acid, Corrosion Science, 46(2004), 2987–3003.

496　[33] A. Pfennig, R. Bäßler, Effect of CO_2 on the stability of steels with 1% and 13% Cr in saline water,

497　　　Corrosion Science, 51(2009),931–940.

498　[34] N. Mundhenk, S. Carrero, K.G. Knauss, R. Wonneberger, A. Undisz, Y. Wu, Kinetic and

499　　　thermodynamic analysis of high-temperature CO2 corrosion of carbon steel in simulated

500　　　geothermal NaCl fluids, Corrosion science, 171(2020), 108597.

501　[35] N. Mundhenk, P. Huttenloch, R. Bäßler, T. Kohl, H. Steger, R. Zorn, Electrochemical study of the

502　　　corrosion of different alloys exposed to deaerated 80°C geothermal brines containing CO_2,

503　　　Corrosion Science, 84(2014), 180.

504　[36] X. H. Lu, G. X. Zhao, J. B. Zhang, et al., Corrosion behavior of super 13Cr martensitic stainless

505　　　steel in CO_2 and H_2S/CO_2 environment, Journal of Beijing University of Science and Technology,

506　　　32(2010), 207-212.

507　[37] OLI Systems, Inc, OLI Analyzer Studio, Vers.3.1, 108 American Road, Morris Plaines, New Jersey

508　　　www.olisystems.com.

509　[38] ASTM G1-03 Standard Practice for Preparing, Cleaning, and Evaluating Corrosion Test Specimens,

510　　　ASTM Int'l, 2011.

511　[39] D.D. Macdonald, A.C. Scott, P. Wentrcek, External reference electrodes for use in high-

512　　　temperature aqueous systems, J. Electrochem. Soc. 126 (1979) 908–911.

513　[40] ASTM G61-86. Standard Test Method for Conducting Cyclic Potentiodynamic Polarization

514　　　Measurements for Localized Corrosion Susceptibility of Iron-, Nickel-, or Cobalt-Based Alloys,

515　　　2009.

516　[41] H. Tian, X. Cheng, Y. Wang, et al., Effect of Mo on interaction between α/γ phases of duplex

517　　　stainless steel, Electrochimica Acta, (2018), S0013468618303736.

518　[42] S. Q. Dong, X. Chen, E. Callagon La Plante, M. Gussev, K. Leonard, G. Sant, Elucidating the grain-

519　　　orientation dependent corrosion rates of austenitic stainless steels, Materials & Design, 191.

520　[43] M.C. Biesinger, B.P. Payne, A.P. Grosvenor, L.W. Lau, A.R. Gerson, R.S.C. Smart, Resolving surface

521　　　chemical states in XPS analysis of first row transition metals, oxides and hydroxides: Cr, Mn, Fe,

522　　　Co and Ni, Appl. Surf. Sci. 257 (2011) 2717–2730.

523　[44] Y.L. Han, J.N. Mei, Q.J. Peng, E.-H. Han, W. Ke, Effect of electropolishing on corrosion of Alloy

600 in high temperature water, Corrosion Science, 98 (2015), 72–80.

[45] Y. Zhao, J. Xie, G. Zeng, T. Zhang, D. Xu, F. Wang, Pourbaix diagram for HP-13Cr stainless steel in the aggressive oilfield environment characterized by high temperature, high CO2 partial pressure and high salinity, Electrochim. Acta, 293 (2019), 116–127.

[46] Y. Zhao, X. Li, C. Zhang, T. Zhang, J. Xie, G. Zeng, D. Xu, F. Wang, Investigation of the rotation speed on corrosion behavior of HP-13Cr stainless steel in the extremely aggressive oilfield environment by using the rotating cage test, Corrosion Science, 145(2018), 307–319.

[47] Z. Zhu, X. Liu, Z. Ye, J. Zhang, F. Cao, J. Zhang, A fabrication of iridium oxide film pH micro-sensor on Pt ultramicroelectrode and its application on in-situ pH distribution of 316L stainless steel corrosion at open circuit potential, Sens. Actuators B Chem, 255(2018),1974–1982.

[48] J. Bischoff, A. T. Motta, Oxidation behavior of ferritic–martensitic and ODS steels in supercritical water, Journal of Nuclear Materials, 424(2012), 261-276.

[49] J. Z. Wang, J. Q. Wang, h. L. Ming, Z. M. Zhang, E. H. Han, Effect of temperature on corrosion behavior of alloy 690 in high temperature hydrogenated water, Journal of Materials Science & Technology, 34(2018), 1419-1427.

[50] J. Robertson, The mechanism of high temperature aqueous corrosion of stainless steels, Corrosion Science, 32(1991), 443-465.

[51] W. Kuang, X. Wu, E. H. Han, J. Rao. Effect of alternately changing the dissolved Ni ion concentration on the oxidation of 304 stainless steel in oxygenated high temperature water, Corrosion Science, 53(2011), 2582-2591.

[52] W. Kuang, X. Wu, E. H. Han, L. Ruan, Effect of nickel ion from autoclave material on oxidation behaviour of 304 stainless steel in oxygenated high temperature water, Corrosion Science, 53(2011), 1107-1114.

[53] J. Xu, X. Q. Wu, E. H. Han, The evolution of electrochemical behaviour and oxide film properties of 304 stainless steel in high temperature aqueous environment, Electrochimica Acta, 71(2012), 219-226.